

Rapid-adiabatic-passage-based super-resolution microscopy in semiconductor quantum dot system

Partha Das^{1,*}, Samit Kumar Hazra^{1,†} and Tarak Nath Dey^{1,‡}

¹*Department of Physics, Indian Institute of Technology Guwahati, Guwahati 781039, Assam, India*

We theoretically investigate rapid adiabatic passage(RAP)-based super-resolution imaging in a two-level quantum dot system interacting with two structured beams. To understand the physical mechanism behind the formation of super-resolution for the experiment of Kaldewey *et. al.*, [Nature Photonics 10.1038/s41566-017-0079-y (2018)], we first use Liouville's density matrix where photon-mediated radiative and non-radiative decays are incorporated. A suitably chosen spatiotemporal envelope of the structured beams enables the formation of a super-resolution image. We also find that the feature size of the image depends on the intensity of the Laguerre Gaussian beam(LG). However, the created image resolution undergoes distortion due to the existence of a low-intensity circular ring. The unwanted circular ring arises from the dominance of the LG beam tail over the super-Gaussian(SG) beam tail, initiating the residual population transfer from the ground state to the excited state. This limitation can be overcome by using the Bessel-modulated truncated structured LG and SG beams. We next study the dynamics of the semiconductor quantum dot system at finite temperatures wherein the phonon interaction becomes imperative. We employ the polaron-transformed master equation to explore the system at higher temperatures. Our numerical results confirm that the sharpness of the image remains intact at low temperatures with weak phonon coupling. Hence, the proposed scheme may open up applications in nano-scale imaging with quantum dots.

I. INTRODUCTION

Conventional optics fail to resolve the spot size of an image beyond a value comparable to the probing light wavelength. Ernst Abbe first realized that the primary constraint of resolution imaging comes from diffraction [1]. Later it was mathematically formulated using Fourier transform theory [2]. Defeating the diffraction barrier has been the key to achieving high-resolution imaging. The use of super-resolution microscopy can overcome the diffraction. The realization of super-resolution microscopy is possible due to the advent of the photolithography technique. In this technique, Scott et al. [3] and Andrew et al. [4] have used photochromic molecules as a mask to imprint a nanoscale pattern on a target material. The mask shows a dramatic response to light interaction. The opaque mask becomes transparent in the presence of the writing beam with wavelength λ_1 , whereas it becomes opaque again by applying inhibitor beam light with wavelength λ_2 . Exploiting these fascinating properties of the mask, they created a nanosize pattern using a writing Gaussian beam and an inhibitor Laguerre-Gaussian (LG) beam. The concept of switching between transparent and opaque has been successfully realized in stimulated emission-depletion (STED) microscopy for nanosize particle imaging [5, 6]. In STED microscopy, excitation and depletion light beams are used to illuminate the sample simultaneously. The excitation beam excites the fluorescent molecules to the bright state, and the depletion beam turns them back to the dark

state by stimulated emission. The transition probability between bright and dark states depends on the intensity of the laser beam. Therefore, the depletion beam, which has a doughnut intensity profile, can image only the fluorophores in the small central area where the beam intensity is zero. STED microscopy has opened up a new platform for imaging at the nanoscale, in material science and medical biology [7, 8]. In particular, STED involves fluorescence depletion, which is an incoherent process. There are also other contemporary techniques [9, 10] which give an incoherent response to the laser.

RAP based imaging can further improve the shortfall of STED microscopy. The RAP exploits the coherent response of the laser [11], which indicates coherent manipulation of quantum states to achieve efficient population transfer. It uses a time-advance strong RAP positive chirping pulse that transfers the population from the ground to the excited state. A second time-delayed RAP pulse with negative chirping can de-excite the population from the excited state to the ground state. Hence, the intensity-dependent RAP in a two-level system acts like a nearly ideal 'on' and 'off' switch, which qualifies the critical criterion of super-resolution microscopy. With the advent of short, intense pulse and pulse-shaping technology, selective population transfer has become efficient. Population transfer through a chirp pulse is much more effective than the pulse without chirping [12]. Moreover, a frequency-swept pulse-induced excitation is immune from Rabi oscillation [13, 14]. Under the adiabatic condition, a strong Rabi frequency can transfer the population at the desired level without decay and decoherence inducing losses [15].

Semiconductor quantum dots (QDs) allow precise control over their size, shape, and composition, enabling more tailored RAP implementation than atomic systems

* partha.2015@iitg.ac.in

† samit176121009@iitg.ac.in

‡ tarak.dey@iitg.ac.in

[16]. It explores the effect of coherent control and decoherence in solid-state systems. Experiments on optically driven InGaAs/GaAs QDs found the intensity damping of Rabi rotation due to longitudinal acoustic (LA) phonons [17, 18]. These self-assembled QDs interact with the phonons, limiting the excitonic transition's coherence [19–25]. Various theoretical approaches have been proposed for investigating phonon interaction's role in the excited state's coherent population distribution. This includes the master equation (ME) using perturbative expansion of the exciton-phonon coupling in Markovian [17, 18, 22, 26] and non-Markovian limit [19, 27, 28], numerical techniques with path integral method [21], and correlation expansion [20, 29, 30].

In this work, we provide a detailed theoretical study for the recent experiments on super-resolution imaging in QDs [11]. The experiments were performed in InGaAs QD embedded in GaAs. The strong confinement of charge carriers of the QDs brings about discrete energy levels to mimic an atomic medium. We first use the density matrix equation for two-level system to explain the formation of the spot size beyond the diffraction limit. We show how a truncated spatial envelope of the Bessel-modulated SG and Bessel-modulated LG beam can improve the spot size resolution by stopping residual ground state population excitation. In QD's, longitudinal acoustic phonon interaction is inevitable because of the environment temperature. The interactions between phonon and exciton greatly influence the exciton-photon interaction. Therefore, investigating phonon-mediated dephasing is mandatory for image formation. To illustrate the effect of temperature on imaging, we further study the polaron master equation. We find that the image formation degrades with the increase in temperature. Hence a lower temperature with weak electron-phonon coupling is favourable to form a sharp image. These tunable optical properties of QD find application in sensors, drug delivery, biomedical imaging [31, 32], quantum communication, and quantum information [33].

The paper is organized as follows. Section I contains a brief introduction to super-resolution and its application in the QD medium. In section II we present the level system and theoretical formalism without taking the phonon contribution. In section III we discuss the numerical results. Section IV contains the inclusion of a phonon bath interacting with QD by using the polaron master equation. In section V we present the result including the phonon-induced dephasing. Finally, in section VI, we give a conclusion of the work.

II. THEORETICAL FORMULATION

A. Level system

Controllable population transfer at the excited state is the essence behind super-resolution imaging. A variety of methods, such as stimulated Raman adiabatic pas-

sage (STIRAP), super-adiabatic STIRAP (saSTIRAP), and rapid adiabatic passage (RAP), have been used to transfer the population to the desired state. The population inversion is beyond reach for a two-level system due to the thermodynamic limit. RAP can overcome this limitation. The two-level system can achieve an efficient and robust time-dependent population inversion under the RAP. Based on RAP, super-resolution imaging is demonstrated by Kaldewey *et al.* in an ensemble of QD [11]. This intriguing technique can resolve each QD with a spot size of 30 nm ($\lambda/31$). Inspired and motivated by this experiment, we provide a detailed theoretical explanation for forming super-resolution imaging beyond the diffraction limit based on a full-density matrix and polaron-transformed master equations. The charge confinement of electron-hole pairs leads to semiconductor QD manifests an atom-like discrete energy level structure. A left-handed circularly polarized light that drives the excited (exciton) state $|1\rangle$ and ground state $|2\rangle$ with energy separation $\hbar\omega_{QD}$ produces a two-level configuration as shown in Fig. 1. The incident light consists of two spatiotemporal beams of opposite chirping interacting with the two-level quantum dot by the induced dipole moment. We have adopted a semi-classical treatment of light-matter interaction where the field is classical, and the energy levels of QD are discrete. The excitation and de-excitation of two beams which couple the states $|1\rangle$ and $|2\rangle$ are respectively given as

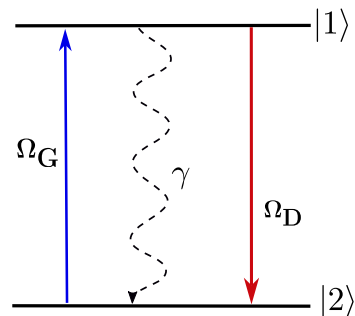


FIG. 1. Schematic diagram of two-level quantum dot system. Two spatiotemporal beams interact with the system of Rabi frequencies Ω_G and Ω_D . The spontaneous emission decay rate from $|1\rangle$ to $|2\rangle$ is given by γ . The two beams interact resonantly with both the levels.

$$\vec{E}_G(r, t) = \hat{\sigma}_- E_G(r) \exp \left[-\frac{t^2}{2\tau^2} - i\omega_G t - i\alpha_G \frac{t^2}{2} \right] + \text{c.c.}, \quad (1a)$$

$$\vec{E}_D(r, t) = \hat{\sigma}_- E_D(r) \exp \left[-\frac{t^2}{2\tau^2} - i\omega_D t - i\alpha_D \frac{t^2}{2} \right] + \text{c.c.}, \quad (1b)$$

where $\hat{\sigma}_-$ is the left circular polarization unit vector, τ is chirped pulse width, ω_G and ω_D are the corresponding carrier frequencies, α_G and α_D are the linear temporal chirp of the first and second pulse respectively. Specifically, the linear temporal chirp denotes the sweep rate of

the laser from a negative detuning to a positive detuning or vice-versa. The spatial profiles of the two beams $E_G(r)$ and $E_D(r)$ are taken to be a SG and LG₀¹, respectively, expressed as

$$E_G(r) = E_G^0 \exp \left[- \left(\frac{r^2}{2w_G^2} \right)^2 \right], \quad (2a)$$

$$E_D(r) = E_D^0 \left(\frac{r}{w_D} \right) \exp \left[- \left(\frac{r^2}{2w_D^2} \right) \right] \exp[i\phi], \quad (2b)$$

where E_G^0 and E_D^0 are the amplitude, and the beam waist of each beam is denoted by w_G and w_D , and ϕ is the phase difference between the two beams, which we have taken $\phi = \pi/2$. The SG beam transfers the population from the ground state to the excited state, and the LG beam depletes the excited state population to the ground state. In the presence of the two beams, the time-dependent Hamiltonian of the system under electric dipole approximation is given as

$$\mathbf{H} = \mathbf{H}_0 + \mathbf{H}_I, \quad (3a)$$

$$\mathbf{H}_0 = \hbar\omega_{QD}|1\rangle\langle 1|, \quad (3b)$$

$$\mathbf{H}_I = -\vec{d}_{12} \cdot \left(\vec{E}_G(r, t) + \vec{E}_D(r, t) \right) |1\rangle\langle 2| + \text{H.c.}, \quad (3c)$$

where $\vec{d}_{12} = \langle 1|\hat{d}|2\rangle$ is the matrix elements of the induced dipole moment operator \hat{d} for the transition $|1\rangle \leftrightarrow |2\rangle$. We make a unitary transformation as

$$\mathbf{U} = e^{-i\nu(t)t|1\rangle\langle 1|}, \quad (4)$$

where $\nu(t) = \omega_D + \alpha_D t/2$. Note that the time-dependent frequency signifies the characteristics of the chirp pulse. Now, the effective Hamiltonian in the interaction picture is given by

$$\mathcal{H}_{eff} = \mathbf{U}^\dagger \mathbf{H} \mathbf{U} - i\hbar \mathbf{U}^\dagger \frac{\partial \mathbf{U}}{\partial t}. \quad (5)$$

Under rotating wave approximation (RWA) the above Hamiltonian gives

$$\begin{aligned} \mathcal{H}_{eff} = & -\hbar\Delta(t)|1\rangle\langle 1| - \frac{\hbar}{2}(\Omega_G(r, t)e^{i\delta(t)t} + \Omega_D(r, t))|1\rangle\langle 2| \\ & - \frac{\hbar}{2}(\Omega_G^*(r, t)e^{-i\delta(t)t} + \Omega_D^*(r, t))|2\rangle\langle 1|, \end{aligned}$$

where the detunings are defined as

$$\Delta(t) = (\omega_D + \alpha_D t) - \omega_{QD}, \quad (6a)$$

$$\delta(t) = (\omega_D - \omega_G) - \frac{t}{2}(\alpha_G - \alpha_D). \quad (6b)$$

Both the beams interact resonantly with two-level system *i.e.*, $\omega_D = \omega_G = \omega_{QD}$. The spatiotemporal Rabi frequencies of respective beams are

$$\Omega_G = \Omega_G^0 \exp \left[- \left(\frac{r^2}{2w_G^2} \right)^2 \right] \exp \left[- \frac{t^2}{2\tau^2} \right], \quad (7a)$$

$$\Omega_D = i\Omega_D^0 \left(\frac{r}{w_D} \right) \exp \left[- \left(\frac{r^2}{2w_D^2} \right) \right] \exp \left[- \frac{t^2}{2\tau^2} \right], \quad (7b)$$

where the amplitudes are given as, $\Omega_G^0 = \vec{d}_{12} \cdot \hat{\sigma}_- E_G^0 / \hbar$ and $\Omega_D^0 = \vec{d}_{12} \cdot \hat{\sigma}_- E_D^0 / \hbar$.

B. Density Matrix Equations

In general, the population in the excited state can decay through radiative or non-radiative processes. This decay mechanism not only changes the population of the excited state but also modifies the atomic coherences. So, to study the system dynamics, we must incorporate damping terms. To do this, we use the following Liouville equation:

$$\frac{\partial \rho}{\partial t} = -\frac{i}{\hbar} [\mathcal{H}_{eff}, \rho] + \mathcal{L}\rho. \quad (8)$$

The last term of Eq.(8) represents radiative and nonradiative processes that can be determined by

$$\mathcal{L}\rho = -\frac{\gamma}{2}(|1\rangle\langle 1|\rho - 2|2\rangle\langle 1|\rho|1\rangle\langle 2| + \rho|1\rangle\langle 1|), \quad (9)$$

where γ is the radiative decay rate of the excited state. The equations of motion for the populations and coherences of the two-level system are expressed as

$$\begin{aligned} \dot{\rho}_{11} = & \frac{i}{2}(\Omega_D + \Omega_G e^{i\delta(t)t})\rho_{21} - \frac{i}{2}(\Omega_D^* + \Omega_G^* e^{-i\delta(t)t})\rho_{12} \\ & - \gamma\rho_{11} \end{aligned} \quad (10a)$$

$$\begin{aligned} \dot{\rho}_{22} = & -\frac{i}{2}(\Omega_D + \Omega_G e^{i\delta(t)t})\rho_{21} + \frac{i}{2}(\Omega_D^* + \Omega_G^* e^{-i\delta(t)t})\rho_{12} \\ & + \gamma\rho_{11} \end{aligned} \quad (10b)$$

$$\dot{\rho}_{12} = -\left(\frac{\gamma}{2} - i\Delta(t)\right)\rho_{12} + \frac{i}{2}(\Omega_D + \Omega_G e^{i\delta(t)t})(\rho_{22} - \rho_{11}) \quad (10c)$$

$$\dot{\rho}_{21} = \dot{\rho}_{12}^* \quad (10d)$$

where the overdots signify time derivatives and star (*) denotes the complex conjugates. The diagonal elements, ρ_{ii} , ($i \in 1, 2$) of the density matrix follow the conservation of population, *i.e.*, $\rho_{11} + \rho_{22} = 1$.

C. RAP in two-level system

Besides spectroscopy, it is of profound importance to prepare a specific quantum state in semiconductors for different fields like quantum computation [34, 35], single and entangled photons [36, 37], Bose-Einstein condensation[38]. RAP is an advantageous way to prepare a state as it remains insensitive to the variation of the laser field intensity or the pulse area beyond the adiabatic threshold. The population change between the two-level atomic states can happen in two distinct adiabatic ways. To understand the two processes, we use the well-known dressed state (adiabatic state) eigenvectors of a time-dependent Hamiltonian of a two-level system

interacting with a chirp pulse of Rabi frequency Ω_1 is given as [39]

$$|\psi_+(t)\rangle = \sin\theta(t)|2\rangle + \cos\theta(t)|1\rangle, \quad (11a)$$

$$|\psi_-(t)\rangle = \cos\theta(t)|2\rangle - \sin\theta(t)|1\rangle, \quad (11b)$$

where the instantaneous eigenstates are the linear superposition of the bare states (diabatic state). The mixing angle $\theta(t)$ between the states is defined by

$$\sin 2\theta = \frac{|\Omega_1(t)|}{\sqrt{\Delta_1(t)^2 + |\Omega_1(t)|^2}}, \quad (12a)$$

$$\cos 2\theta = \frac{\Delta_1(t)}{\sqrt{\Delta_1(t)^2 + |\Omega_1(t)|^2}}, \quad (12b)$$

where $\Delta_1(t)$ is the time-dependent detuning. We can also, obtain the eigenvalues of the dressed state which are given by

$$E_{\pm} = \frac{\hbar}{2} \left[\Delta_1(t) \pm \sqrt{\Delta_1(t)^2 + |\Omega_1(t)|^2} \right]. \quad (13)$$

Indeed, we can write the Hamiltonian in the adiabatic basis as

$$H_a = \hbar \begin{bmatrix} E_- & -i\dot{\theta} \\ i\dot{\theta} & E_+ \end{bmatrix}. \quad (14)$$

The adiabatic condition requires that the maximum rate of change in the adiabatic states, $|\psi_{\pm}\rangle$ must be smaller than the minimum difference between the eigenvalues. Thus the adiabatic condition reads

$$|\dot{\theta}(t)| \ll |E_+(t) - E_-(t)|. \quad (15)$$

Now for the case of (i) constant detuning, we can infer from Eq. (13) that the energies of the dressed states remain parallel to each other long before and after the interaction with a pulsed laser. Only during the pulse interaction time, the states are in the superposition of the bare states. Therefore, in this case, the population completely return to its initial state, which is the no-crossing scenario of adiabatic evolution. In another case of (ii) time-dependent detuning, *i.e.*, when the frequency sweeps adiabatically from a large negative value to a large positive value (or vice versa) two limits arise, (a) for large negative detuning ($|\Omega_1(t)| \ll |\Delta_1(t)|$),

$$\begin{aligned} E_+ &\rightarrow 0; & E_- &\rightarrow -\hbar\Delta_1, \\ |\psi_+\rangle &\rightarrow |2\rangle; & |\psi_-\rangle &\rightarrow -|1\rangle, \end{aligned} \quad (16)$$

and (b) for large positive detuning ($|\Omega_1(t)| \ll |\Delta_1(t)|$),

$$\begin{aligned} E_+ &\rightarrow \hbar\Delta_1; & E_- &\rightarrow 0, \\ |\psi_+\rangle &\rightarrow |1\rangle; & |\psi_-\rangle &\rightarrow |2\rangle. \end{aligned} \quad (17)$$

Both the two limits assert that the initial population in state $|2\rangle$ adiabatically follows $|\psi_+\rangle$ during the frequency-swept and finally makes an inversion to state $|1\rangle$. This is called the avoided crossing or anticrossing in adiabatic evolution. It is also called rapid as the process should occur shorter than the lifetime of the excited state.

III. NUMERICAL RESULTS

A. RAP-based spot formation

Under the adiabatic condition, a two-level system interacting with a Gaussian chirp pulse can robustly transfer the population from one state to another. We have

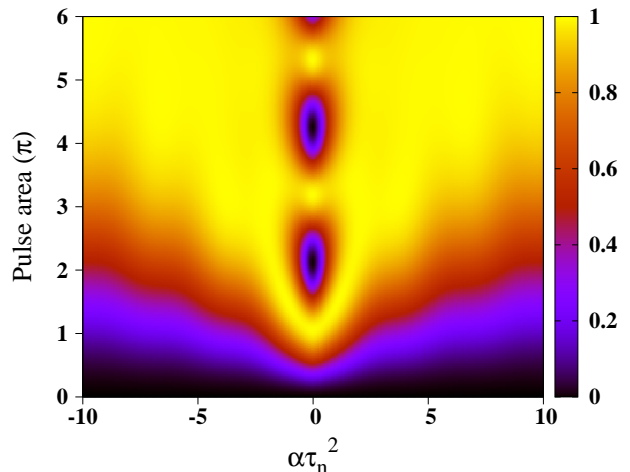


FIG. 2. Excited state population as a function of pulse area and chirping. The color bar denotes the population of the excited state.

used two such sequential Gaussian chirp pulses with opposite chirping. To perform the computation with the

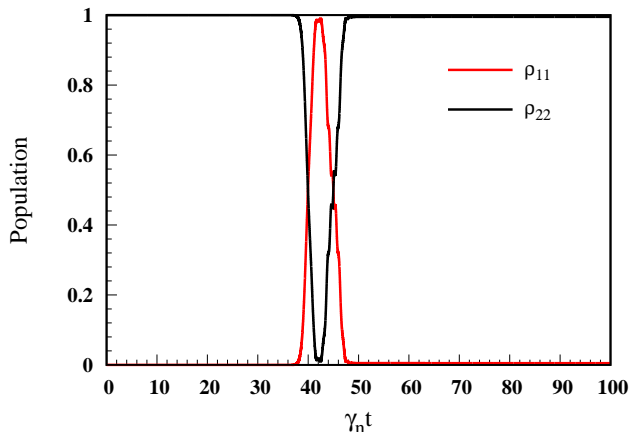


FIG. 3. Population transfer via RAP. The first pulse with positive chirp of 3.24 ps^{-2} and pulse area greater than π transfers the population to the excited state and the subsequent pulse with chirp -3.24 ps^{-2} and pulse area greater than π bring down the excited state population to ground state. Both the pulse has a width $1.37\tau_n$.

system parameters, we need to normalize it to a dimen-

sionless quantity. We have chosen the normalized frequency $\gamma_n = 1 \text{ ps}^{-1}$ and time $\tau_n = 1/\gamma_n$. In Fig. 2, we have plotted the excited state population as a function of the pulse area and chirp (α) of the pulse. We find if there is no chirp ($\alpha\tau_n^2 = 0$), we get the usual Rabi oscillation *i.e.*, for the odd multiple of π the population transfer to the excited state whereas for even multiple of π it remains in the ground state. Also, we notice that robust population transfer can happen due to RAP for several parameters that satisfy the conditions, $|\alpha|\tau_n^2 \gg 1$ and $|\alpha|\tau_n^2 \ll \Omega_0^2\tau_n^2$. Here Ω_0 is the peak Rabi frequency of the chirped pulse. As in Fig. 3, the first pulse peaked at $t\gamma_n = 40$, Rabi frequency $\Omega_G^0 = 4.0\gamma_n$, positive chirp $\alpha_G = 3.24 \text{ ps}^{-2}$ and having pulse area $> \pi$ takes the population to the excited state that was initially in the ground state. The next pulse is peaked at $t\gamma_n = 45$, Rabi fre-

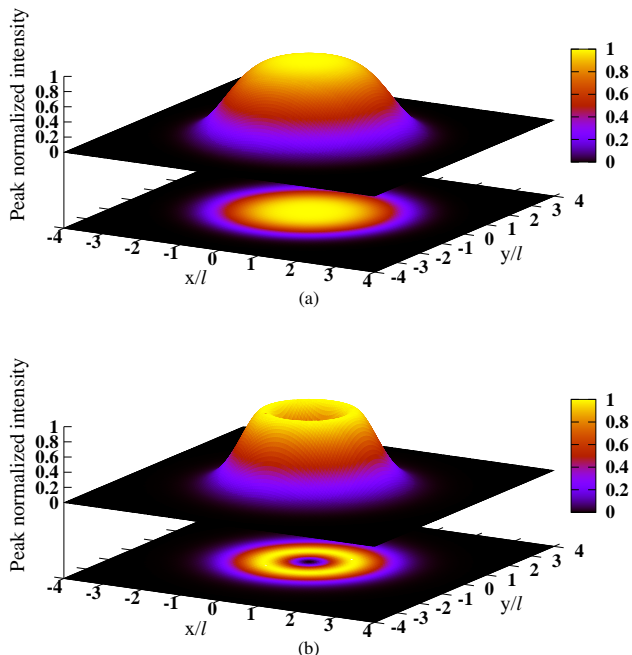


FIG. 4. The 3-D intensity distribution of (a) SG beam of width $1.7l$ and (b) LG spatiotemporal beam of width $1.0l$

quency $\Omega_D^0 = 10.4\gamma_n$, with a negative chirp $\alpha_D = -3.24 \text{ ps}^{-2}$ which returns back the population to the ground state. The spontaneous decay rate of the excited state $\gamma = 800 \text{ ps}^{-1}$. The second pulse is implemented in a short interval of the first to make the population return efficiently so that the two pulses act like an on-off switch. This efficient population transfer and return is crucial for imaging based on this scheme. The frequency-swept is adiabatic so that $\Omega_0^2 \gg |d\Delta/dt|$.

Now for RAP-based imaging, the system is driven by two spatiotemporal beams with SG and LG spatial profiles shown in Figs. 4(a) and 4(b) respectively. The SG and LG beam waists are $1.7l$ and $1.0l$, respectively. Here l is a characteristic length defined by $l = f/(k\sigma)$. The lens

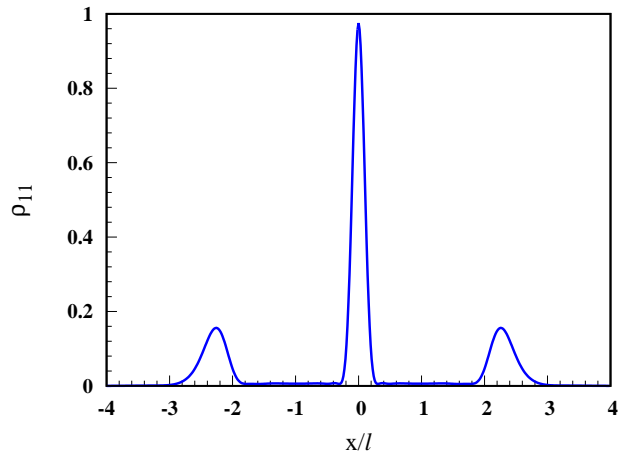


FIG. 5. Population of the excited state vs. spatial extent in QD system. The applied spatiotemporal beams SG has waist $w_G = 1.7l$, and LG has waist $w_D = 1.0l$. The spatial distribution of the excited state population is shown at $\gamma_n t = 60$. Other parameters are the same as in Fig. 3.

's focal length is 3.7 mm ., the wavevector $k = 2\pi n/\lambda$. We take the refractive index of the gallium phosphide (GaP) solid emersion lens, $n = 3.5$, and wavelength of the laser $\lambda = 940 \text{ nm}$. The spatial extent of the beam before focusing on a lens is taken as $\sigma = 1.2 \text{ mm}$. So, the characteristic length l becomes 131.86 nm . This can be regarded as the beam's spot size when it is focused through a lens for the above parameters. The Rabi frequency of the SG beam is $\Omega_G^0 = 4.0\gamma_n$ and for the LG beam, is $\Omega_D^0 = 10.4\gamma_n$. Successively implementing SG and LG spatiotemporal beams produce a spot size of $\Delta x_{\text{FWHM}}/l = 0.2$ *i.e.*, 26.37 nm . In Fig. (5), we show the excited state population distribution at $\gamma_n t = 60$. Other than the cen-

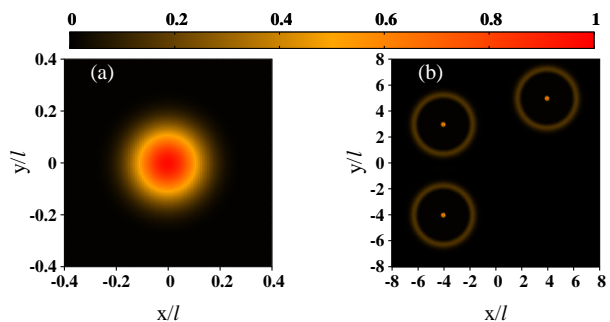


FIG. 6. The 2-D spot size of (a) single QD emitter at $(0,0)$. The outer ring is at a higher radius which is not shown here, (b) Multiple emitters at a preassigned position $(-4,-4)$ bottom left, $(-4,3)$ top left and $(4,5)$ top right. Here we can see the low intense outer rings. The parameters are the same as in Fig. 5.

tral peak, small side peaks appear due to the population transition to the excited state due to the LG beam. The tail of the SG beam fails to take all the population to

the excited state, leaving it partially in the ground state. However, the LG beam partially takes this leftover population to an excited state. We have elaborated on the discussion of the occurrence of the side peaks due to the variation of field intensities in the latter part. We choose the beam waist judiciously so that the side peaks remain minimum and far apart from the central maximum. Figure 6(a) shows the central spot in the 2d plane. Also, we can detect multiple QDs at different preassigned locations given in Fig. 6(b). Thus, applying the SG and

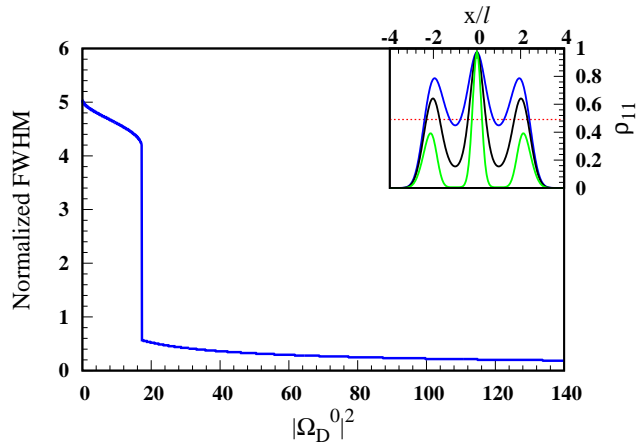


FIG. 7. FWHM of the spot is plotted against the intensity of the spatiotemporal LG beam. The inset shows the excited state population for different LG intensities. The blue, black, and green solid lines correspond to $|\Omega_D^0|^2 = 4, 9, 25$ respectively. The red dotted line represents half of the central maximum.

LG beams successively give a smaller spot size of the QDs emitters.

Next, we analyzed the dependence of the FWHM of the QD spot with the intensity of the LG beam in Fig. 7. The flat top portion of the SG beam, which exists between the spatial range $x/l = \pm 1$, takes all population from the ground state to the excited state. The central peak develops due to the population presence in the excited state at the center $x/l = 0$, where the intensity of the LG beam becomes zero. This is true for taking the orbital angular momentum index as 1 (LG_0^1) in Eq. (2b). This point singularity is the key to achieving sharp resolution at the QD center. The intensity peaks of the LG beam appear at $x/l = \pm 1$, leading to stimulated emission from the excited state to the ground state. Subsequently, a dip is observed in the excited state population ρ_{11} as shown in the inset of Fig. 7. The central peak accompanied by shallow dips gives rise to a larger FWHM. By increasing the LG beam's intensity, the spatial distribution of the excited state population at $x/l = \pm 1$ goes to zero very sharply. Hence, the inset of Fig. 7 reveals the reason behind the narrow spot size formation, which can be made possible by the doughnut beam-assisted complete excited state depopulation. Before the sharp fall of the FWHM the doughnut beam intensity is very low. By

slowly increasing the doughnut beam intensity and keeping the SG beam fixed, much of the population transfers to the ground state. In this context, the peak after the dip in the excited state population occurs due to tail of the LG beam where the intensity is lower than $x/l = \pm 1$. The inset of Fig. 7 (blue and black solid lines) illustrates these phenomena. The red dotted line in the inset of Fig. 7 represents half of the central maximum, and the green solid line displays a typical case of having a side peak below half of the central maximum. It is to be noted that arbitrary enhancement of the intensity up to a larger extent is prohibited because of photobleaching or may even damage the live sample [40, 41]. Now we explain the occurrence of side peaks due to the field intensities variation along the transverse plane. In Fig. 8, the black solid line represents the spot size which is the same as Fig. 5. This has the lowest side peak for $\Omega_G^0 = 4.0\gamma_n$ and $\Omega_D^0 = 10.4\gamma_n$. Increasing the intensity of the LG beam's spatiotemporal envelope reduces the central spot intensity, enhancing and shifting the side peak intensities to a larger spatial extent. This procedure leads to more residual ground state population transfer to the excited state. All the solid lines in Fig. 8 give evidence of this phenomenon. Moreover, increasing the SG spatiotempo-

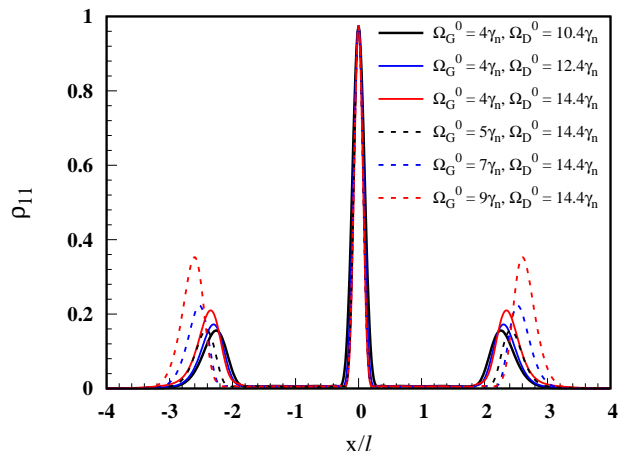


FIG. 8. Dependence of beam intensity on spot formation. The solid lines correspond to the field value where the SG value is constant varying the LG intensity, and the dotted lines are vice-versa.

ral beam intensity transfers much of the population to the excited state from the ground state. This population returns to the ground state accompanied by the LG beam. Due to this, the side peak (black, blue dotted lines) slightly shifts in Fig. 8. As the intensity of the SG beam surpasses the intensity of the LG beam, even though much of the population transfer to the excited state, the excited state population partially returns to the ground state. Thus there is a sharp rise of the side peak (red dotted line). All the dashed lines in Fig. 8 suggest the scenario where the SG beam intensity is varied, keeping the LG beam intensity at a fixed value. It is im-

portant to note that we have used SG and LG beams of opposite chirping for state transfer protocol. This fact is unambiguously explained by Eq. (16),(17) in the context of RAP.

B. Reduction of side peak

It is evident from the previous analysis that the formation of side peaks around the central maximum of the QD spot is inevitable by considering the fields whose spatial envelopes represent by Eqs. (1a) and (1b). Even though these side peaks are small, these peaks may degrade the resolution where several QDs emitters within the specific range. So, finding the modulated fields that will decrease the side peak nearly to zero is pertinent. A complete sup-

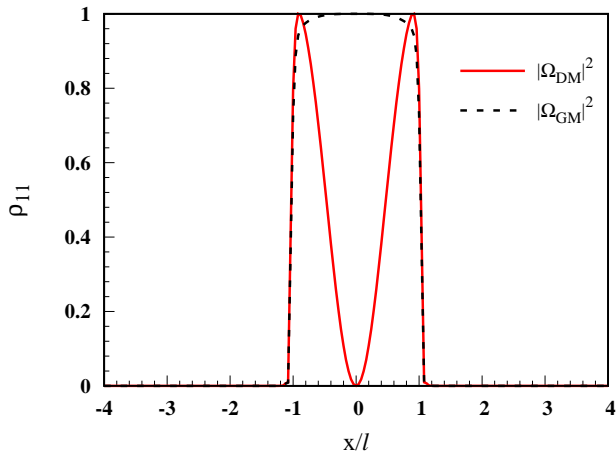


FIG. 9. Normalized peak intensities of Bessel-modulated SG and Bessel-modulated LG beam are plotted against spatial extent. The red solid line, and the black dotted line correspond to the modulated LG and SG beams, respectively. Both the beams are truncated at $x/l = 1.2$. Other parameters are the same as in Fig. 4.

pression of residual ground state population flow is possible by considering the truncated beams which are formed by the Bessel-modulated SG and Bessel-modulated LG beams given as

$$\vec{E}_{GM}(r, t) = \vec{E}_G(r, t) [a_1 J_0(r^{16}) + a_2 J_2(r^{16})], \quad (18a)$$

$$\vec{E}_{DM}(r, t) = \vec{E}_D(r, t) [b_1 J_0(r^{16}) + b_2 J_2(r^{16})]. \quad (18b)$$

Here $J_i(i \in 0, 2)$ is the Bessel function of the first kind with order i , a_i and b_i are modulation coefficients (real numbers) which we have chosen, $a_1 = a_2 = 1.5$, $b_1 = b_2 = 1.0$. The modified Rabi frequencies of modulated LG and SG beams are Ω_{DM} , Ω_{GM} respectively. In Fig. 9, the two modulated beams are truncated at $x/l = \pm 1.2$, which can be obtained experimentally by finite apertures. The modulated SG beam takes all the population from the ground state to the excited state. Due to the sharp fall of the modulated SG intensity at

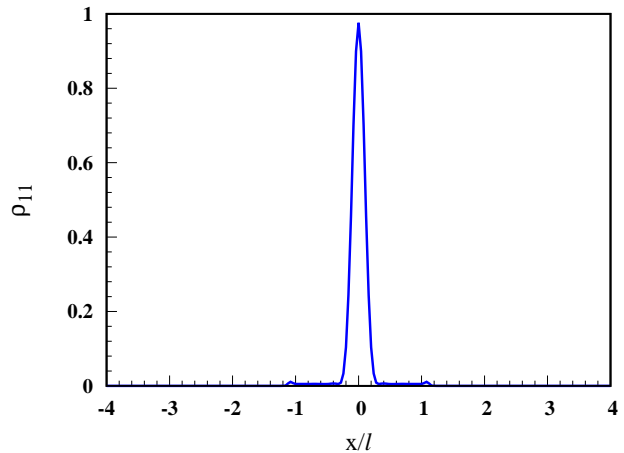


FIG. 10. The modified population of the excited state is plotted as a function of the spatial extent. The modulated fields in Fig. 9 result in reducing the side peak to almost zero. Other parameters are the same as in Fig. 5

$x/l = \pm 1.2$, the ground state population beyond the spatial range, $x/l = 0$ to $x/l = \pm 1.2$ cannot be excited to the excited state. Similarly, the excited state population goes through stimulated emission by the modulated LG beam keeping only the population at the center $x/l = 0$, which is shown in Fig. 10. Keeping the spot size of the QD emitter the same as Fig. 5, we can reduce the side peak nearly to zero.

IV. EFFECT OF EXCITON-PHONON COUPLING

The system under consideration is significantly different from the well-studied single-atom emitters due to the solid-state nature of the semiconductor QD emitters. The medium consists of a few InGaAs QDs grown on top of GaAs host material using molecular beam epitaxy. Therefore the host lattice vibration modifies the QD dynamics depending on the environment temperature. In the literature, the quantized form of the vibrational energy in a periodic structure refers to a phonon. Many theoretical and experimental studies confirm the longitudinal acoustic (LA) phonon coupling with QDs via deformation potential. Therefore, various new quantum phenomena were discovered, like the appearance of new features in Mollow triplets [42, 43], emission line broadening [20, 44, 45], and limiting degree of indistinguishability of photons [46, 47]. On the other hand, the QD-phonon interaction model explains several quantum features, such as Rabi rotation [26], rapid adiabatic passage [48–50], and phonon-assisted state preparation [51, 52]. Hence, the previous model is only suitable for weak QD-phonon coupling at near-absolute-zero temperatures. It is pertinent to include the effect of phonon, interacting with the two-level QD configuration. The system is coupled

to an acoustic phonon bath represented by as a collection of harmonic oscillators with frequency $\omega_m = c_s k$ where, c_s is the velocity of sound and k is the wavevector, creation and annihilation operator of the m^{th} mode are b_m^\dagger and b_m respectively. The coupling constant for exciton phonon mode is λ_m . So, the effective Hamiltonian in the interaction picture can be written as [53],

$$\begin{aligned} \mathbf{H}_I(t) = & \frac{\hbar}{2}(\Omega(t)|1\rangle\langle 2| + \Omega(t)^*|2\rangle\langle 1|) - \hbar\Delta|1\rangle\langle 1| \\ & + \sum_m \hbar\omega_m b_m^\dagger b_m + \sum_m \hbar\lambda_m(b_m + b_m^\dagger)|1\rangle\langle 1| \end{aligned} \quad (19)$$

where Δ is given by Eq. (6a) and the complex Rabi frequency $\Omega(t) = \Omega_D + \Omega_G e^{i\delta t}$. We make a transformation to polaron frame to get the polaron-transformed Hamiltonian

$$H_P = e^P H_I e^{-P}, \text{ where } P = |1\rangle\langle 1| \sum_m \frac{\lambda_m}{\omega_m} (b_m^\dagger - b_m)$$

This transformed Hamiltonian gives the freedom to split the total Hamiltonian into system, bath, and interaction parts which are given as [54, 55],

$$H_S = -\hbar\Delta|1\rangle\langle 1| + \langle B \rangle X_g(t) \quad (20a)$$

$$H_B = \sum_m \hbar\omega_m b_m^\dagger b_m \quad (20b)$$

$$H_I = X_g(t)\zeta_g + X_u(t)\zeta_u. \quad (20c)$$

The phonon-modified system operators can be defined as follows:

$$X_g(t) = \frac{\hbar}{2}(\Omega|1\rangle\langle 2| + \Omega^*|2\rangle\langle 1|)$$

$$X_u(t) = \frac{i\hbar}{2}(\Omega|1\rangle\langle 2| - \Omega^*|2\rangle\langle 1|)$$

The fluctuation operators induced by the bath are $\zeta_g = (B_+ + B_- + 2\langle B \rangle)/2$, $\zeta_u = (B_+ - B_-)/2i$. The phonon displacement operator can be expressed as

$$B_\pm = \exp \left[\pm \sum_m \frac{\lambda_m}{\omega_m} (b_m^\dagger - b_m) \right]$$

The displacement operators contain summation over all the phonon modes, we can average it out for a particular temperature T as, $\langle B_+ \rangle = \langle B_- \rangle \equiv \langle B \rangle$. The expectation value is given by,

$$\langle B \rangle = \exp \left[-\frac{1}{2} \int_0^\infty \frac{J(\omega)}{\omega^2} \coth \left(\frac{\hbar\omega}{2k_B T} \right) d\omega \right] \quad (21)$$

where k_B is the Boltzmann constant, $J(\omega) = \alpha_p \omega^3 \exp[-\omega^2/2\omega_b^2]$ is called the phonon spectral function where α_p and ω_b are the electron-phonon coupling strength and the phonon cutoff frequency, respectively.

To study the dynamics of the system interacting with the phonon we use the ME using polaron transformed Hamiltonian where the interaction Hamiltonian is treated

as a perturbation. The Born-Markov approximation is made to the Hamiltonian to describe the system dynamics in the presence of the phonon bath [54, 55]. Further simplification is made by using Markov approximation since phonon relaxation time is much shorter than the system dynamics [55]. Including the radiative and dephasing rates we obtain full polaron ME as,

$$\frac{\partial \rho}{\partial t} = -\frac{i}{\hbar}[H_S, \rho] + \frac{\gamma}{2}\mathcal{L}[\sigma^-]\rho + \frac{\gamma'}{2}\mathcal{L}[\sigma^+\sigma^-]\rho + \mathcal{L}_{ph}\rho \quad (22)$$

where $\sigma^+ = |1\rangle\langle 2|$, $\sigma^- = |2\rangle\langle 1|$ are raising and lowering operators of the system respectively. The Lindblad superoperator, $\mathcal{L}[\hat{O}]\rho = 2\hat{O}\rho\hat{O}^\dagger - \hat{O}^\dagger\hat{O}\rho - \rho\hat{O}^\dagger\hat{O}$ acting on a operator \hat{O} . The radiative decay and dephasing are denoted by γ and γ' , respectively. The term \mathcal{L}_{ph} includes phonon bath in system dynamics is given by,

$$\begin{aligned} \mathcal{L}_{ph} = & -\frac{1}{\hbar^2} \int_0^\infty \sum_{l=g,u} \{G_l(\tau)[X_l(t), X_l(t, \tau)\rho(t)] \\ & + H.c.\} d\tau \end{aligned} \quad (23)$$

where, $X_l(t, \tau) = e^{-iH_S\tau/\hbar} X_l(t) e^{iH_S\tau/\hbar}$ and the polaron Green functions are,

$$G_g(\tau) = \langle B \rangle^2 \{ \cosh[\phi(\tau)] - 1 \} \quad (24a)$$

$$G_u(\tau) = \langle B \rangle^2 \sinh[\phi(\tau)] \quad (24b)$$

which depend on the phonon correlation function which is,

$$\phi(\tau) = \int_0^\infty \frac{J(\omega)}{\omega^2} \left[\coth \left(\frac{\hbar\omega}{2k_B T} \right) \cos(\omega\tau) - i \sin(\omega\tau) \right] d\omega \quad (25a)$$

This full polaron ME is generally valid in the range,

$$\left(\frac{\Omega}{\omega_b} \right)^2 (1 - \langle B \rangle^4) \ll 1 \quad (26)$$

which enables us to investigate the effect of phonons in weak coupling with strong field as well as strong coupling with weak field limit. After performing the commutation algebra and we get a simplified form with different decay rates associated with various phonon-induced processes. So, Eq. (23) reduced to,

$$\begin{aligned} \frac{\partial \rho}{\partial t} = & -\frac{i}{\hbar}[H_S, \rho] + \frac{\gamma}{2}\mathcal{L}[\sigma^-]\rho + \frac{\gamma'}{2}\mathcal{L}[\sigma^+\sigma^-]\rho \\ & + \frac{\Gamma^{\sigma^+}}{2}\mathcal{L}[\sigma^+]\rho - \Gamma^{cd}(\sigma^+\rho\sigma^+ + \sigma^-\rho\sigma^-) \\ & + \frac{\Gamma^{\sigma^-}}{2}\mathcal{L}[\sigma^-]\rho - i\Gamma^{sd}(\sigma^+\rho\sigma^+ - \sigma^-\rho\sigma^-) \\ & + i\Delta^{\sigma^+\sigma^-}[\sigma^+\sigma^-, \rho] - [i\Gamma_{gu+}(\sigma^+\sigma^-\rho\sigma^+ + \sigma^-\rho \\ & - \sigma^+\sigma^-\rho\sigma^-) + H.c.] - [\Gamma_{gu-}(\sigma^+\sigma^-\rho\sigma^+ - \sigma^-\rho \\ & + \sigma^+\sigma^-\rho\sigma^-) + H.c.] \end{aligned} \quad (27)$$

The scattering terms Γ^{cd+} , Γ^{cd-} correspond to cross-dephasing rates [56], $\Gamma^{\sigma+}$ and $\Gamma^{\sigma-}$ describe the phonon-assisted incoherent excitation and an enhanced radiative decay process respectively. The emission of phonon transfers the system from a higher energy state to a lower energy state whereas, phonon absorption takes the system from a lower energy state to a higher energy state. These processes are temperature dependent. At low temperature phonon emission process is more favorable than the absorption process. As the temperature increases the radiative decay also increases and both the scattering rates become nearly equal.

V. RESULT: INCLUDING PHONON-INDUCED DECOHERENCE

The phonon-induced decay rates will affect the population distribution among the QD states for different temperatures. To study the dependence we have solved the simplified analytical ME in Eq. (27) where all the decoherence rates are taken into account. We have taken

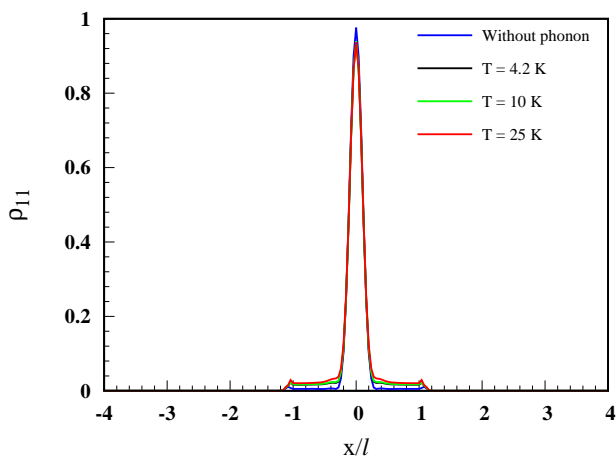


FIG. 11. Spot size for low coupling $\alpha_p = 2 \times 10^{-3} \text{ ps}^2$ and higher field intensity. The truncated beams (Eqs. (18a), 18b) having $\Omega_G^0 = 4.0\gamma_n$, $\Omega_D^0 = 10.4\gamma_n$, $a_1 = a_2 = 1.5$, $b_1 = b_2 = 1.0$. The phonon cutoff frequency $\omega_b = 1 \text{ meV}$, $\gamma = \gamma' = 2 \mu\text{eV}$. Other parameters are the same as in Fig. 5.

the additional parameters for InGaAs/GaAs QDs which are used in [52]. The phonon cutoff frequency $\omega_b = 1 \text{ meV}$, and we choose $\gamma = \gamma' = 2 \mu\text{eV}$. As earlier we have normalized the parameters to dimensionless quantity by choosing $\gamma_n = 1 \text{ ps}^{-1}$. The validity of our ME allows us to investigate the weak and strong phonon coupling for certain temperatures with higher and lower field intensity respectively. In the first case, we have taken the Rabi frequency of truncated SG $\Omega_G^0 = 4.0\gamma_n$ and truncated LG $\Omega_D^0 = 10.4\gamma_n$ which weakly coupled to the phonon bath as, $\alpha_p = 2 \times 10^{-3} \text{ ps}^2$ with modulation coefficients, $a_1 = a_2 = 1.5$, $b_1 = b_2 = 1.0$, and the rest parameters are same as previously taken. We find due to weak

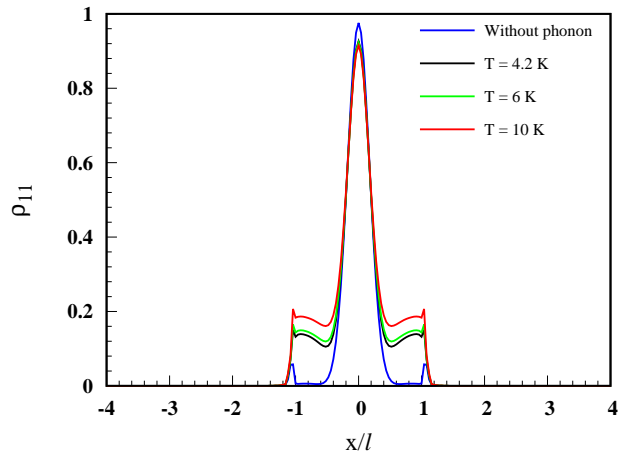


FIG. 12. Spot size for higher coupling $\alpha_p = 3 \times 10^{-2} \text{ ps}^2$ and low-intense fields. The truncated SG beam having $\Omega_G^0 = 2\gamma_n$, chirping 1.51 ps^{-2} , $\tau = 1.7\tau_n$, and the truncated LG beam having $\Omega_D^0 = 4\gamma_n$, chirping -1.51 ps^{-2} , $\tau = 1.7\tau_n$. The modulation coefficients are $a_1 = b_1 = 1.0$, $a_2 = 1.6$, $b_2 = 1.4$. Other parameters are the same as in Fig. 11.

coupling there is negligible distortion in the spot size as shown in Fig. 11. Whereas in the second case, we consider strong coupling, $\alpha_p = 3 \times 10^{-2} \text{ ps}^2$ for chirping 1.51 ps^{-2} and the Rabi frequency of the truncated SG beam is $\Omega_G^0 = 2\gamma_n$ and for the truncated LG beam is $\Omega_D^0 = 4\gamma_n$ with modulation coefficients, $a_1 = b_1 = 1.0$, $a_2 = 1.6$, $b_2 = 1.4$ which is much weaker than the former case. We see that at large coupling the spot size gets distorted which highly diminishes the sharpness of the spot as in Fig. 12. Although it has been reported in [57] about the decoupling of phonons in much higher pulse areas our theory deals with much shorter pulses restricted by the validity condition mentioned earlier, we find that the increase in temperature distorts the spot adequately. Also in both cases, we observe a decrease in population in the central spot due to the phonon decoherence. As we see from the above discussion the phonon-induced decoherence rates deform the QD spot depending on the coupling strength. This hindrance to resolution is due to inefficient population transfer among the quantum states. So, even though the modulated truncated beams can able to minimize the side peak to the maximum extent the above analysis shows that a lower temperature with weak electron-phonon coupling is favorable for resolution measurement. Hence, the polaron-transformed ME gives an overall understanding of super-resolution in solid-state QDs.

VI. CONCLUSION

In conclusion, we have theoretically studied RAP-based imaging in semiconductor QD systems. For this purpose, we have adopted a semi-classical treatment for

describing the spatiotemporal beams that interact with the two-level QD system. We use dressed state analysis to understand the RAP-assisted population transfer in the presence of chirping pulses. We also show how the QD emitter's spot size depends on the LG field intensity. The compromise of image resolution in an ensemble of dense QDs because of the circular ring. The dominant character of the LG beam tail over the SG beam tail causes residual population flow from the ground state to the excited state, creating the circular ring. Further, we have used the modulated truncated beams to over-

come the image distortion. The phonon vibration in a semiconductor quantum dot system is inevitable at finite temperatures. To encompass the temperature-dependent phonon-induced decoherence rates for super-resolution imaging formation, we explore full polaron ME. Our analysis reveals that sharp image formation is possible at finite low temperatures with weak electron-phonon coupling. However, the QD emitter's spot size gets distorted at substantial high temperatures. Hence, this investigation may have potential applications in nano-scale imaging, with scalability and controllability.

APPENDIX: Polaron Master Equation Derivation

In this Appendix, we give the derivation of analytically obtained scattering rates for the phonon-mediated scattering processes. The full-polaron ME is,

$$\frac{\partial \rho}{\partial t} = \frac{1}{i\hbar} [H_S(t), \rho(t)] + \frac{\gamma}{2} \mathcal{L}[\sigma^-] \rho + \frac{\gamma'}{2} \mathcal{L}[\sigma^+ \sigma^-] \rho + \mathcal{L}_{ph} \rho, \quad (\text{A.1})$$

where, \mathcal{L}_{ph} is given by,

$$\mathcal{L}_{ph} \rho = -\frac{1}{\hbar^2} \int_0^\infty \sum_{l=g,u} d\tau \{G_l(\tau) [X_l(t), X_l(t, \tau) \rho(t)] + H.c.\}. \quad (\text{A.2})$$

Here, $X_l(t, \tau) = e^{-iH_S(t)\tau/\hbar} X_l(t) e^{iH_S(t)\tau/\hbar}$. Now, the modified system operators are given below. Note that the time dependent field with Rabi frequency, $\Omega(t) = \Omega_D + \Omega_G e^{i\delta t}$ couples with QD system.

$$X_g(t) = \frac{\hbar}{2} (\Omega(t) \sigma^+ + \Omega(t)^* \sigma^-) \quad (\text{A.3})$$

$$= \frac{\hbar}{2} \{ \text{Re}[\Omega(t)] (\sigma^+ + \sigma^-) - i \text{Im}[\Omega(t)] (\sigma^- - \sigma^+) \} \quad (\text{A.4})$$

$$= \frac{\hbar}{2} \{ \text{Re}[\Omega(t)] \sigma_x - \text{Im}[\Omega(t)] \sigma_y \} \quad (\text{A.5})$$

and

$$X_u(t) = \frac{i\hbar}{2} (\Omega(t) \sigma^+ - \Omega(t)^* \sigma^-) \quad (\text{A.6})$$

$$= -\frac{\hbar}{2} \{ \text{Im}[\Omega(t)] (\sigma^+ + \sigma^-) + i \text{Re}[\Omega(t)] (\sigma^- - \sigma^+) \} \quad (\text{A.7})$$

$$= -\frac{\hbar}{2} \{ \text{Im}[\Omega(t)] \sigma_x + \text{Re}[\Omega(t)] \sigma_y \}. \quad (\text{A.8})$$

Also the polaron Green's functions are

$$G_g(\tau) = \langle B \rangle^2 \{ \cosh[\phi(\tau)] - 1 \} \quad \text{and} \quad G_u(\tau) = \langle B \rangle^2 \sinh[\phi(\tau)]. \quad (\text{A.9})$$

The full polaron-transformed system Hamiltonian $H_S = -\hbar\Delta |1\rangle\langle 1| + \langle B \rangle X_g(t)$. Using Born-Markov approximation, the two-time phonon system operators can be written in terms of the one-time operators in the interaction picture.

$$X_g(t, \tau) = e^{-iH_S(t)\tau/\hbar} X_g(t) e^{iH_S(t)\tau/\hbar} \quad (\text{A.10})$$

$$X_u(t, \tau) = e^{-iH_S(t)\tau/\hbar} X_u(t) e^{iH_S(t)\tau/\hbar} \quad (\text{A.11})$$

So, we get the following,

$$X_g(t, \tau) = \frac{\hbar}{2} \left\{ \left[\frac{\text{Re}[\Omega(t)] (\Delta^2 \cos[\eta(t)\tau] + |\Omega_R(t)|^2)}{\eta(t)^2} - \frac{\text{Im}[\Omega(t)] (\Delta \sin[\eta(t)\tau])}{\eta(t)} \right] \sigma_x - \frac{2\Delta \langle B \rangle |\Omega(t)|^2 (1 - \cos[\eta(t)\tau])}{\eta(t)^2} \right. \\ \left. \times \sigma^+ \sigma^- - \left[\frac{\text{Im}[\Omega(t)] (\Delta^2 \cos[\eta(t)\tau] + |\Omega_R(t)|^2)}{\eta(t)^2} + \frac{\text{Re}[\Omega(t)] (\Delta \sin[\eta(t)\tau])}{\eta(t)} \right] \sigma_y \right\}, \quad (\text{A.12})$$

$$X_u(t, \tau) = -\frac{\hbar}{2} \left\{ \left[\frac{\text{Re}[\Omega(t)](\Delta \sin[\eta(t)\tau])}{\eta(t)} + \text{Im}[\Omega(t)]\cos[\eta(t)\tau] \right] \sigma_x + \left[\text{Re}[\Omega(t)]\cos[\eta(t)\tau] - \frac{\text{Im}[\Omega(t)](\Delta \sin[\eta(t)\tau])}{\eta(t)} \right] \right. \\ \left. \times \sigma_y + \frac{2\langle B \rangle |\Omega(t)|^2 \sin[\eta(t)\tau]}{\eta(t)} \sigma^+ \sigma^- \right\}, \quad (\text{A.13})$$

where $\eta(t) = \sqrt{|\Omega_R(t)|^2 + \Delta^2}$ and $\Omega_R(t) = \langle B \rangle \Omega(t)$. Now from Eqn (A.2) we get

$$\mathcal{L}_{ph\rho} = -\frac{1}{\hbar^2} \int_0^\infty \{G_g(\tau)[X_g(t), X_g(t, \tau)\rho(t)] + \text{H.c.} + G_u(\tau)[X_u(t), X_u(t, \tau)\rho(t)] + \text{H.c.}\} d\tau. \quad (\text{A.14})$$

Now putting the values of $X_g(t, \tau)$ and $X_u(t, \tau)$ and considering the following definition of real parameters,

$$f(t, \tau) = \frac{\Delta^2 \cos[\eta(t)\tau] + |\Omega_R(t)|^2}{\eta(t)^2}, \quad (\text{A.15})$$

$$g(t, \tau) = \frac{\Delta \sin[\eta(t)\tau]}{\eta(t)}, \quad (\text{A.16})$$

$$h(t, \tau) = \frac{2\Delta\langle B \rangle |\Omega(t)|(1 - \cos[\eta(t)\tau])}{\eta(t)^2}, \quad (\text{A.17})$$

$$q(t, \tau) = \cos[\eta(t)\tau], \quad (\text{A.18})$$

$$r(t, \tau) = \frac{2\langle B \rangle |\Omega(t)|^2 \sin[\eta(t)\tau]}{\eta(t)}, \quad (\text{A.19})$$

we can get

$$\mathcal{L}_{ph\rho} = -\frac{1}{4} \int_0^\infty \left\{ G_g(\tau) \left[(\text{Re}[\Omega(t)]\sigma_x - \text{Im}[\Omega(t)]\sigma_y), \left((\text{Re}[\Omega(t)]f(t, \tau) - \text{Im}[\Omega(t)]g(t, \tau))\sigma_x - (\text{Im}[\Omega(t)]f(t, \tau) \right. \right. \right. \\ \left. \left. + \text{Re}[\Omega(t)]g(t, \tau)\sigma_y - h(t, \tau)\sigma^+ \sigma^- \right) \rho(t) \right] + \text{H.c.} + G_u(\tau) \left[(\text{Im}[\Omega(t)]\sigma_x + \text{Re}[\Omega(t)]\sigma_y), - \left((\text{Re}[\Omega(t)]g(t, \tau) \right. \right. \right. \\ \left. \left. + \text{Im}[\Omega(t)]q(t, \tau)\sigma_x + (\text{Re}[\Omega(t)]q(t, \tau) - \text{Im}[\Omega(t)]g(t, \tau))\sigma_y + r(t, \tau)\sigma^+ \sigma^- \right) \rho(t) \right] + \text{H.c.} \right\} d\tau. \quad (\text{A.20})$$

After performing the commutation algebra we get,

$$\mathcal{L}_{ph\rho} = \int_0^\infty \left\{ \left[-\frac{|\Omega(t)|^2}{4} (-\text{Re}[G_g(\tau)]f(t, \tau) + \text{Im}[G_g(\tau) + G_u(\tau)]g(t, \tau) - \text{Re}[G_u(\tau)]q(t, \tau))\mathcal{L}[\sigma^+] \rho \right] + \left[-\frac{|\Omega(t)|^2}{4} \right. \right. \\ \left. \left. \times (-\text{Re}[G_g(\tau)]f(t, \tau) - \text{Im}[G_g(\tau) + G_u(\tau)]g(t, \tau) - \text{Re}[G_u(\tau)]q(t, \tau))\mathcal{L}[\sigma^-] \rho \right] - \left[\frac{1}{2} ((\text{Re}[G_u(\tau)]q(t, \tau) \right. \right. \right. \\ \left. \left. - \text{Re}[G_g(\tau)]f(t, \tau))(\text{Re}[\Omega(t)^2] - \text{Im}[\Omega(t)^2]) - 2\text{Re}[\Omega(t)]\text{Im}[\Omega(t)](\text{Re}[G_u(\tau)] - \text{Re}[G_g(\tau)]g(t, \tau)) \right] (\sigma^+ \rho \sigma^+ \right. \\ \left. + \sigma^- \rho \sigma^-) \right] - i \left[\frac{1}{2} ((\text{Re}[G_u(\tau)] - \text{Re}[G_g(\tau))](\text{Re}[\Omega(t)^2] - \text{Im}[\Omega(t)^2])g(t, \tau) + 2\text{Re}[\Omega(t)]\text{Im}[\Omega(t)](\text{Re}[G_u(\tau)]q(t, \tau) \right. \right. \\ \left. \left. - \text{Re}[G_g(\tau)]f(t, \tau)) \right] (\sigma^+ \rho \sigma^+ - \sigma^- \rho \sigma^-) \right] + i \left[\frac{|\Omega(t)|^2}{2} ((\text{Re}[G_g(\tau)] + \text{Re}[G_u(\tau)])g(t, \tau))[\sigma^+ \sigma^-, \rho] \right] - \left[i \frac{1}{4} (\text{Im}[\Omega(t)] \right. \\ \left. \times G_g(\tau)h(t, \tau) + \text{Re}[\Omega(t)]G_u(\tau)r(t, \tau))(\sigma^+ \sigma^- \rho \sigma^+ + \sigma^- \rho - \sigma^+ \sigma^- \rho \sigma^-) + \text{H.c.} \right] - \left[\frac{1}{4} (\text{Re}[\Omega(t)]G_g(\tau)h(t, \tau) \right. \\ \left. - \text{Im}[\Omega(t)]G_u(\tau)r(t, \tau))(\sigma^+ \sigma^- \rho \sigma^+ - \sigma^- \rho + \sigma^+ \sigma^- \rho \sigma^-) + \text{H.c.} \right] \left. \right\}, \quad (\text{A.21})$$

$$\mathcal{L}_{ph\rho} = \frac{\Gamma^{\sigma^+}}{2} \mathcal{L}[\sigma^+] \rho + \frac{\Gamma^{\sigma^-}}{2} \mathcal{L}[\sigma^-] \rho - \Gamma^{cd}(\sigma^+ \rho \sigma^+ + \sigma^- \rho \sigma^-) - i\Gamma^{sd}(\sigma^+ \rho \sigma^+ - \sigma^- \rho \sigma^-) + i\Delta^{\sigma^+ \sigma^-} [\sigma^+ \sigma^-, \rho] \\ - [i\Gamma_{gu+}(\sigma^+ \sigma^- \rho \sigma^+ + \sigma^- \rho - \sigma^+ \sigma^- \rho \sigma^-) + \text{H.c.}] - [\Gamma_{gu-}(\sigma^+ \sigma^- \rho \sigma^+ - \sigma^- \rho + \sigma^+ \sigma^- \rho \sigma^-) + \text{H.c.}], \quad (\text{A.22})$$

where all the phonon-mediated scattering rates which contributes in the Lindblad ME are given below.

$$\begin{aligned}
\Gamma^{\sigma^+} &= -\frac{|\Omega(t)|^2}{2} \int_0^\infty (-\text{Re}[G_g(\tau)]f(t, \tau) + \text{Im}[G_g(\tau) + G_u(\tau)]g(t, \tau) - \text{Re}[G_u(\tau)]q(t, \tau)) d\tau \\
&= \frac{|\Omega_R(t)|^2}{2} \int_0^\infty \left(\text{Re} \left\{ \cosh[\phi(\tau)] - 1 \right\} \left\{ \frac{\Delta^2 \cos[\eta(t)\tau] + |\Omega_R(t)|^2}{\eta(t)^2} \right\} + \sinh[\phi(\tau)]\cos[\eta(t)\tau] \right) - \text{Im}[e^{\phi(\tau)} - 1] \\
&\quad \left\{ \frac{\Delta \sin[\eta(t)\tau]}{\eta(t)} \right\} d\tau, \tag{A.23}
\end{aligned}$$

$$\begin{aligned}
\Gamma^{\sigma^-} &= -\frac{|\Omega(t)|^2}{2} \int_0^\infty (-\text{Re}[G_g(\tau)]f(t, \tau) - \text{Im}[G_g(\tau) + G_u(\tau)]g(t, \tau) - \text{Re}[G_u(\tau)]q(t, \tau)) d\tau \\
&= \frac{|\Omega_R(t)|^2}{2} \int_0^\infty \left(\text{Re} \left\{ \cosh[\phi(\tau)] - 1 \right\} \left\{ \frac{\Delta^2 \cos[\eta(t)\tau] + |\Omega_R(t)|^2}{\eta(t)^2} \right\} + \sinh[\phi(\tau)]\cos[\eta(t)\tau] \right) + \text{Im}[e^{\phi(\tau)} - 1] \\
&\quad \left\{ \frac{\Delta \sin[\eta(t)\tau]}{\eta(t)} \right\} d\tau, \tag{A.24}
\end{aligned}$$

$$\begin{aligned}
\Gamma^{cd} &= \frac{1}{2} \int_0^\infty ((\text{Re}[G_u(\tau)](\tau)q(t, \tau) - \text{Re}[G_g(\tau)]f(t, \tau))(\text{Re}[\Omega(t)^2] - \text{Im}[\Omega(t)^2]) - 2\text{Re}[\Omega(t)]\text{Im}[\Omega(t)](\text{Re}[G_u(\tau)] \\
&\quad - \text{Re}[G_g(\tau)])g(t, \tau)) d\tau \\
&= \frac{1}{2} \int_0^\infty \langle B \rangle^2 \left(\text{Re} \left\{ \sinh[\phi(\tau)]\cos[\eta(t)\tau] - \cosh[\phi(\tau)] - 1 \right\} \left\{ \frac{\Delta^2 \cos[\eta(t)\tau] + |\Omega_R(t)|^2}{\eta(t)^2} \right\} \right) (\text{Re}[\Omega(t)^2] \\
&\quad - \text{Im}[\Omega(t)^2]) - 2\text{Re}[\Omega]\text{Im}[\Omega]\text{Re}[1 - e^{-\phi(\tau)}] \left\{ \frac{\Delta \sin[\eta(t)\tau]}{\eta(t)} \right\} d\tau, \tag{A.25}
\end{aligned}$$

$$\begin{aligned}
\Gamma^{sd} &= \frac{1}{2} \int_0^\infty ((\text{Re}[G_u(\tau)] - \text{Re}[G_g(\tau)])g(t, \tau)(\text{Re}[\Omega(t)^2] - \text{Im}[\Omega(t)^2]) + 2\text{Re}[\Omega(t)]\text{Im}[\Omega(t)](\text{Re}[G_u(\tau)]q(t, \tau) \\
&\quad - \text{Re}[G_g(\tau)]g(t, \tau))) d\tau \\
&= \frac{1}{2} \int_0^\infty \langle B \rangle^2 \left(\text{Re}[1 - e^{-\phi(\tau)}] \left\{ \frac{\Delta \sin[\eta(t)\tau]}{\eta(t)} \right\} (\text{Re}[\Omega(t)^2] - \text{Im}[\Omega(t)^2]) + 2\text{Re}[\Omega(t)]\text{Im}[\Omega(t)]\text{Re} \left\{ \sinh[\phi(\tau)] \right. \right. \\
&\quad \times \left. \left. \cos[\eta(t)\tau] - \cosh[\phi(\tau)] - 1 \right\} \left\{ \frac{\Delta^2 \cos[\eta(t)\tau] + |\Omega_R|^2}{\eta(t)^2} \right\} \right) d\tau, \tag{A.26}
\end{aligned}$$

$$\begin{aligned}
\Delta^{\sigma^+\sigma^-} &= \frac{|\Omega_R(t)|^2}{2} \int_0^\infty \text{Re}([G_g(\tau)] + G_u(\tau))g(t, \tau) d\tau \\
&= \frac{|\Omega_R(t)|^2}{2} \int_0^\infty \text{Re}[e^{\phi(\tau)} - 1] \left(\frac{\Delta \sin[\eta(t)\tau]}{\eta(t)} \right) d\tau, \tag{A.27}
\end{aligned}$$

$$\begin{aligned}
\Gamma_{gu+} &= \frac{1}{4} \int_0^\infty (\text{Im}[\Omega(t)]G_g(\tau)h(t, \tau) + \text{Re}[\Omega(t)]G_u(\tau)r(t, \tau)) d\tau \\
&= \frac{1}{4} \int_0^\infty \left(\text{Im}[\Omega(t)]\cosh[\phi(t)\tau] - 1 \right) \left\{ \frac{2\Delta\langle B \rangle|\Omega(t)|^2(1 - \cos[\eta(t)\tau])}{\eta(t)^2} \right\} + \text{Re}[\Omega(t)]\sinh[\phi(\tau)] \\
&\quad \times \left\{ \frac{2\langle B \rangle|\Omega(t)|^2\sin[\eta(t)\tau]}{\eta(t)} \right\} d\tau, \tag{A.28}
\end{aligned}$$

$$\begin{aligned}
\Gamma_{gu-} &= \frac{1}{4} \int_0^\infty (\text{Re}[\Omega(t)]G_g(\tau)h(t, \tau) - \text{Im}[\Omega(t)]G_u(\tau)r(t, \tau)) d\tau \\
&= \frac{1}{4} \int_0^\infty \left(\text{Re}[\Omega(t)]\cosh[\phi(t)\tau] - 1 \right) \left\{ \frac{2\Delta\langle B \rangle|\Omega(t)|^2(1 - \cos[\eta(t)\tau])}{\eta(t)^2} \right\} - \text{Im}[\Omega(t)]\sinh[\phi(\tau)] \\
&\quad \times \left\{ \frac{2\langle B \rangle|\Omega(t)|^2\sin[\eta(t)\tau]}{\eta(t)} \right\} d\tau. \tag{A.29}
\end{aligned}$$

The above phonon-induced scattering rates are a function of time. At each time t the values are calculated by integrating with respect to τ . These analytically derived scattering rates illustrate the physical picture of electron-phonon coupling in semiconductor QDs.

-
- [1] E. Abbe, *Archiv für Mikroskopische Anatomie* **9**, 413 (1873).
- [2] H. Köhler, *Opt. Acta* **28**, 1691 (1981).
- [3] T. F. Scott, B. A. Kowalski, A. C. Sullivan, C. N. Bowman, and R. R. McLeod, *Science* **324**, 913 (2009).
- [4] T. L. Andrew, H.-Y. Tsai, and R. Menon, *Science* **324**, 917 (2009).
- [5] S. W. Hell, *Nature Biotechnology* **21**, 1347 (2003).
- [6] S. W. Hell, *Science* **316**, 1153 (2007).
- [7] S. W. Hell and J. Wichmann, *Opt. Lett.* **19**, 780 (1994).
- [8] T. Müller, C. Schumann, and A. Kraegeloh, *ChemPhysChem* **13**, 1986 (2012).
- [9] S. Weisenburger and V. Sandoghdar, *Contemporary Physics* **56**, 123 (2015).
- [10] F. Balzarotti, Y. Eilers, K. C. Gwosch, A. H. Gynnå, V. Westphal, F. D. Stefani, J. Elf, and S. W. Hell, *Science* **355**, 606 (2017).
- [11] T. Kaldewey, A. V. Kuhlmann, S. R. Valentin, A. Ludwig, A. D. Wieck, and R. J. Warburton, *Nature Photonics* **12**, 68 (2018).
- [12] V. Malinovsky and J. Krause, *Eur. Phys. J. D* **14**, 147 (2001).
- [13] J. S. Melinger, S. R. Gandhi, A. Hariharan, D. Goswami, and W. S. Warren, *The Journal of Chemical Physics* **101**, 6439 (1994).
- [14] E. R. Schmidgall, P. R. Eastham, and R. T. Phillips, *Phys. Rev. B* **81**, 195306 (2010).
- [15] S. Herbers, Y. M. Caris, S. E. J. Kuijpers, J.-U. Grabow, and S. Y. T. van de Meerakker, *Molecular Physics*, e2129105 (2022).
- [16] A. Ramachandran, J. Fraser-Leach, S. O’Neal, D. G. Deppe, and K. C. Hall, *Opt. Express* **29**, 41766 (2021).
- [17] A. J. Ramsay, A. V. Gopal, E. M. Gauger, A. Nazir, B. W. Lovett, A. M. Fox, and M. S. Skolnick, *Phys. Rev. Lett.* **104**, 017402 (2010).
- [18] A. J. Ramsay, T. M. Godden, S. J. Boyle, E. M. Gauger, A. Nazir, B. W. Lovett, A. M. Fox, and M. S. Skolnick, *Phys. Rev. Lett.* **105**, 177402 (2010).
- [19] P. Machnikowski and L. Jacak, *Phys. Rev. B* **69**, 193302 (2004).
- [20] A. Krügel, V. M. Axt, T. Kuhn, P. Machnikowski, and A. Vagov, *Applied Physics B* **81**, 897 (2005).
- [21] A. Vagov, M. D. Croitoru, V. M. Axt, T. Kuhn, and F. M. Peeters, *Phys. Rev. Lett.* **98**, 227403 (2007).
- [22] A. Nazir, *Phys. Rev. B* **78**, 153309 (2008).
- [23] B. Krummheuer, V. M. Axt, and T. Kuhn, *Phys. Rev. B* **65**, 195313 (2002).
- [24] A. Vagov, V. M. Axt, and T. Kuhn, *Phys. Rev. B* **66**, 165312 (2002).
- [25] A. Grodecka, C. Weber, P. Machnikowski, and A. Knorr, *Phys. Rev. B* **76**, 205305 (2007).
- [26] E. M. Gauger, A. Nazir, S. C. Benjamin, T. M. Stace, and B. W. Lovett, *New Journal of Physics* **10**, 073016 (2008).
- [27] R. Alicki, M. Horodecki, P. Horodecki, R. Horodecki, L. Jacak, and P. Machnikowski, *Phys. Rev. A* **70**, 010501 (2004).
- [28] D. Mogilevtsev, A. P. Nisovtsev, S. Kilin, S. B. Cavalcanti, H. S. Brandi, and L. E. Oliveira, *Phys. Rev. Lett.* **100**, 017401 (2008).
- [29] J. Förstner, C. Weber, J. Danckwerts, and A. Knorr, *Phys. Rev. Lett.* **91**, 127401 (2003).
- [30] A. Krügel, V. M. Axt, and T. Kuhn, *Phys. Rev. B* **73**, 035302 (2006).
- [31] H. M. Gil, T. W. Price, K. Chelani, J.-S. G. Bouillard, S. D. Calaminus, and G. J. Stasiuk, *iScience* **24**, 102189 (2021).
- [32] C. T. Matea, T. Mocan, F. Tabaran, T. Pop, O. Mosteanu, C. Puia, C. Iancu, and L. Mocan, *International Journal of Nanomedicine* **12**, 5421 (2017).
- [33] S. K. Hazra, P. K. Pathak, and T. N. Dey, *Phys. Rev. B* **107**, 235409 (2023).
- [34] D. P. DiVincenzo, *Science* **270**, 255 (1995).
- [35] E. F. et al., *Science* **292**, 472 (2001).
- [36] P. M. et al., *Science* **290**, 2282 (2000).
- [37] R. M. S. et al, *Nature* **439**, 179 (2006).
- [38] P. R. Eastham and R. T. Phillips, *Phys. Rev. B* **79**, 165303 (2009).
- [39] B. W. Shore, M. V. Gromovyy, L. P. Yatsenko, and V. I. Romanenko, *American Journal of Physics* **77**, 1183 (2009).
- [40] W. Zhang, A. Noa, K. Nienhaus, L. Hilbert, and G. U. Nienhaus, *Journal of Physics D: Applied Physics* **52**, 414001 (2019).
- [41] W. Jahr, P. Velicky, and J. G. Danzl, *Methods* **174**, 27 (2020).
- [42] C. Roy and S. Hughes, *Phys. Rev. Lett.* **106**, 247403 (2011).
- [43] S. M. Ulrich, S. Ates, S. Reitzenstein, A. Löffler, A. Forchel, and P. Michler, *Phys. Rev. Lett.* **106**, 247402 (2011).
- [44] L. Besombes, K. Kheng, L. Marsal, and H. Mariette, *Phys. Rev. B* **63**, 155307 (2001).
- [45] E. Stock, M.-R. Dachner, T. Warming, A. Schliwa, A. Lochmann, A. Hoffmann, A. I. Toropov, A. K. Bakarov, I. A. Derebezov, M. Richter, V. A. Haisler, A. Knorr, and D. Bimberg, *Phys. Rev. B* **83**, 041304 (2011).
- [46] A. Thoma, P. Schnauber, M. Gschrey, M. Seifried, J. Wolters, J.-H. Schulze, A. Strittmatter, S. Rodt, A. Carmele, A. Knorr, T. Heindel, and S. Reitzenstein, *Phys. Rev. Lett.* **116**, 033601 (2016).
- [47] J. Iles-Smith, D. P. S. McCutcheon, A. Nazir, and J. Mørk, *Nature Photonics* **11**, 521 (2017).
- [48] S. Lüker, K. Gawarecki, D. E. Reiter, A. Grodecka-Grad, V. M. Axt, P. Machnikowski, and T. Kuhn, *Phys. Rev. B* **85**, 121302 (2012).
- [49] A. Debnath, C. Meier, B. Chatel, and T. Amand, *Phys. Rev. B* **86**, 161304 (2012).
- [50] R. Mathew, E. Dilcher, A. Gamouras, A. Ramachandran, H. Y. S. Yang, S. Freisem, D. Deppe, and K. C. Hall, *Phys. Rev. B* **90**, 035316 (2014).
- [51] P.-L. Ardelt, L. Hanschke, K. A. Fischer, K. Müller, A. Kleinkauf, M. Koller, A. Bechtold, T. Simmet, J. Wierzbowski, H. Riedl, G. Abstreiter, and J. J. Finley, *Phys. Rev. B* **90**, 241404 (2014).
- [52] J. H. Quilter, A. J. Brash, F. Liu, M. Glässl, A. M. Barth, V. M. Axt, A. J. Ramsay, M. S. Skolnick, and A. M. Fox, *Phys. Rev. Lett.* **114**, 137401 (2015).
- [53] R. Manson, K. Roy-Choudhury, and S. Hughes, *Phys. Rev. B* **93**, 155423 (2016).
- [54] D. P. S. McCutcheon and A. Nazir, *New Journal of Physics* **12**, 113042 (2010).

- [55] C. Roy and S. Hughes, Phys. Rev. B **85**, 115309 (2012).
- [56] A. Ulhaq, S. Weiler, C. Roy, S. M. Ulrich, M. Jetter, S. Hughes, and P. Michler, Opt. Express **21**, 4382 (2013).
- [57] T. Kaldewey, S. Lüker, A. V. Kuhlmann, S. R. Valentin, J.-M. Chauveau, A. Ludwig, A. D. Wieck, D. E. Reiter, T. Kuhn, and R. J. Warburton, Phys. Rev. B **95**, 241306 (2017).